The Astrophysical Journal Letters, 1000:L38 (15pp), 2026 April 1 https://doi.org/10.3847/2041-8213/ae4b3b

Direct Spectroscopic Confirmation of the Young Embedded Protoplanet WISPIT 2c

Chloe Lawlor[1,2], Richelle F. van Capelleveen[3], Guillaume Bourdarot[4], Christian Ginski[1,2], Matthew A. Kenworthy[3], Tomas Stolker[3], Laird Close[5], Alexander J. Bohn[3], Frank Eisenhauer[4,6], Paulo Garcia[7,8], Sebastian F. Hönig[9], Jens Kammerer[10], Laura Kreidberg[11], Sylvestre Lacour[12], Jean-Baptiste Le Bouquin[13], Eric Mamajek[14], Mathias Nowak[12], Thibaut Paumard[12], Christian Straubmeier[15], and Nienke van der Marel[3]
The ExoGRAVITY Collaboration
[1] School of Natural Sciences, Center for Astronomy, University of Galway, Galway, H91 CF50, Ireland; chloelawlor766@gmail.com
[2] Ryan Institute, University of Galway, Galway, H91 TK33, Ireland
[3] Leiden Observatory, Leiden University, Postbus 9513, 2300 RA Leiden, The Netherlands
[4] Max Planck Institute for Extraterrestrial Physics, Gießenbachstraße 1, 85748 Garching, Germany
[5] Center for Astronomical Adaptive Optics, Department of Astronomy, University of Arizona, 933 N. Cherry Avenue, Tucson, AZ 85718, USA
[6] Department of Physics, Technical University of Munich, 85748 Garching, Germany
[7] Faculdade de Engenharia, Universidade do Porto, rua Dr. Roberto Frias, 4200-465 Porto, Portugal
[8] CENTRA—Centro de Astrofísica e Gravitação, IST, Universidade de Lisboa, 1049-001 Lisboa, Portugal
[9] School of Physics and Astronomy, University of Southampton, Southampton, SO17 1BJ, UK
[10] European Southern Observatory, Karl-Schwarzschild-Straße 2, 85748 Garching, Germany
[11] Max Planck Institute for Astronomy, Königstuhl 17, 69117 Heidelberg, Germany
[12] LIRA, Observatoire de Paris, Université PSL, CNRS, Sorbonne Université, Université de Paris, 5 place Jules Janssen, 92195 Meudon, France
[13] Univ. Grenoble Alpes, CNRS, IPAG, 38000 Grenoble, France
[14] Jet Propulsion Laboratory, California Institute of Technology, 4800 Oak Grove Drive, Pasadena, CA 91109, USA
[15] 1st Institute of Physics, University of Cologne, Zülpicher Straße 77, 50937 Cologne, Germany
Received 2025 December 15; revised 2026 February 23; accepted 2026 February 25; published 2026 March 24

Abstract

WISPIT 2 is a nearby young star with a multiringed disk that was recently confirmed to host a ∼4.9 $M_{\rm Jup}$ gas giant planet embedded in a large (60 au) gap at a radial separation of 57 au from the host star. We confirm and characterize a second, close-in planet in the WISPIT 2 system using a combination of new Very Large Telescope/SPHERE *H*-band dual-polarization imaging and VLTI/GRAVITY *K*-band interferometric observations of the WISPIT 2 system. The GRAVITY detection is consistent with a point-like source while its extracted *K*-band spectrum shows CO band-head absorption at 2.3 μm and a continuum shape consistent with a young giant planet. From the GRAVITY data, we extract a medium resolution *K*-band spectrum of the companion and fit atmospheric model grids using the `species` tool with nested sampling to constrain its effective temperature, radius, and luminosity. We infer $T_{\rm eff}$ of 1500–2600 K, a radius of 0.91–2.2 $R_{\rm Jup}$, and a luminosity of (−3.47)–(−3.63). Comparison with evolutionary tracks implies a mass range of 8–12 $M_{\rm Jup}$, approximately twice as massive as the previously confirmed WISPIT 2b. The astrometry rules out a background source and marginally detects orbital motion of WISPIT 2 c, which needs further follow-up observations for confirmation. WISPIT 2 now becomes an analog to PDS 70, offering a second laboratory for studying the formation and early evolution of a multiplanet system within its natal disk.

Unified Astronomy Thesaurus concepts: Protoplanetary disks (1300); Exoplanets (498); Exoplanet formation (492); Direct imaging (387); Interferometry (808); Spectroscopy (1558)

1. Introduction

The detection of thousands of extrasolar planets with indirect detection methods indicates that planet formation is an efficient process that happens commonly around young stars (see, e.g., J. J. Lissauer et al. 2023). At the same time, high-resolution observations of planet-forming disks at multiple wavelengths have now revealed intricate substructures in more than a hundred systems (see the recent surveys by S. M. Andrews et al. 2018; H. Avenhaus et al. 2018; K. I. Öberg et al. 2021; A. Garufi et al. 2024; C. Ginski et al. 2024).

This indicates that planet formation is indeed ongoing in many of these systems, yet the direct detection of embedded planets has proven challenging (e.g., see the discussion in J. Milli et al. 2012; T. Currie et al. 2023). While there are mechanisms that can shape transitional disks without requiring the presence of planets (P. S. Marcus et al. 2015; M. Flock et al. 2017; N. T. Kurtovic et al. 2018; S. S. Suriano et al. 2018; A. Kuznetsova et al. 2022), many of these systems provide strong indirect evidence for ongoing planet formation. To date, there are only a few such young, disk-bearing systems in which planets or strong candidates have been confirmed, such as PDS 70 (M. Keppler et al. 2018; S. Y. Haffert et al. 2019), AB Aur (T. Currie et al. 2022), and HD 169142 (I. Hammond et al. 2023). It is the detection of these planets in formation that gives us key insights into the primary formation mechanisms that are at work in the earliest phases of system evolution, be it through core accretion (J. B. Pollack et al. 1996) or gravitational instability (A. P. Boss 1997).

Recently, the WISPIT 2 system has been added to the short list of confirmed planet-bearing disks (L. M. Close et al. 2025a); R. F. van Capelleveen et al. 2025). Uniquely among systems with a confirmed embedded planet, the planet-forming disk in the WISPIT 2 system shows an extended multiple-ringed structure. The primary star in the system is a young solar analog (R. F. van Capelleveen et al. 2025) of $5.1^{+2.4}_{-1.3}$ Myrs,

Table 1
Log of the GRAVITY and SPHERE Observations

Target	UTC Date	Instrument	Setup	NEXP/NDIT/DIT	Air Mass	τ_0 (ms)	Seeing (arcsec)
WISPIT 2	2025-10-05	VLTI/GRAVITY	MEDIUM	12/8/30 s	1.1-1.3	3.1-5.1	0.51–0.79
HD 180595 (CAL)	2025-10-05	VLTI/GRAVITY	MEDIUM	1/32/3 s	1.6	4.3	0.59
WISPIT 2	2025-09-24	VLT/SPHERE	*H* band	48/1/64 s	1.2 ± 0.1	5.7 ± 1.2	0.8 ± 0.2

Table 2
Apparent Magnitudes and Relative Astrometry of WISPIT 2 c

Instrument	UTC Date	Band	Magnitude	Separation (mas)	Position Angle (deg)	References
MagAO-X	2025-04-16	z'	$19.40^{+0.65}_{-0.26}$	109.7 ± 2.9	192.0 ± 1.0	(L. M. Close et al. 2025a)
LBTI/LMIRcam	2025-06-05	*L*	$14.80^{+0.76}_{-0.43}$	113.0 ± 14.0	191.9 ± 2.4	(L. M. Close et al. 2025a)
VLT/SPHERE	2025-03-21	*H*	16.40 ± 0.39	97.69 ± 7.42	198.38 ± 3.85	This work
VLT/SPHERE	2025-09-24	*H*	16.25 ± 0.29	111.45 ± 7.39	193.99 ± 5.25	This work
VLTI/GRAVITY	2025-10-05	*K*	16.04 ± 0.01	105.44 ± 0.03	196.00 ± 0.02	This work

based on stellar isochrones, which gives the intriguing possibility to observe the earliest formation history around a system similar to our own. The embedded planet within the system is located between the innermost two rings at a semimajor axis of 57^{+8}_{-3} au and is estimated to have a mass of $4.9^{+0.9}_{-0.6}\,M_{\rm Jup}$ (R. F. van Capelleveen et al. 2025). The presence of up to four confirmed rings with intermediate gaps, as well as a central cavity in the system, gave rise to speculation that this could be a multiplanet system in formation, possibly comparable to PDS 70, or a younger version of HR 8799 (C. Marois et al. 2008). Indeed, L. M. Close et al. (2025a) pointed out that a signal (referred to as companion candidate CC1) appears to be present in their *L*- and z'-band observations at a projected separation of ∼15 au within the central disk cavity. In this Letter, we present new observations of this companion candidate using the Very Large Telescope (VLT)/Spectro-Polarimetric High-contrast Exoplanet REsearch (SPHERE; J.-L. Beuzit et al. 2019) and VLTI/GRAVITY (GRAVITY Collaboration et al. 2017), confirming the presence of a second planet in the WISPIT 2 system.

2. Observations

In addition to the observations presented in R. F. van Capelleveen et al. (2025), we obtained new high-angular resolution data with both the VLT/SPHERE Infrared Dual-band Imager and Spectrograph (IRDIS; K. Dohlen et al. 2008) and VLTI/GRAVITY, providing up-to-date *H*-band images and *K*-band interferometry observations, respectively.

2.1. Gravity Observations

The GRAVITY observations (GRAVITY Collaboration et al. 2017) were carried out on the four Unit Telescopes (UT) on 2025 October 5. The observations were executed in Service Mode (program ID: 115.29HG.001) with good-to-average atmospheric conditions and a spectral resolution of $R \sim 500$. The log of the observations is included in Table 1. The GRAVITY observations were obtained in dual-field on-axis mode. In this mode, the fringe-tracker (FT) fiber stabilizes the fringes on the host star, and the science channel (SC) fiber alternates between the planet and the star (GRAVITY Collaboration et al. 2019). The pointing of the SC fiber was informed by the SPHERE *H*-band images and with an initial guess at ΔR.A., ΔDecl. = (−22.87 mas, −107.6 mas) from the host star. These observations benefit from the GRAVITY+ extreme Adaptive Optics system (GPAO; GRAVITY+ Collaboration 2025) to reduce the speckle noise close in to the host star and maximize the flux injected in the planet, using the high-order correction with the Natural Guide Star sensor (G. Bourdarot et al. 2024). The data were reduced using the ESO GRAVITY pipeline (V. Lapeyrere et al. 2014). The observations were taken together with an interferometric calibrator in order to measure normalized visibilities. We used the `ExoGRAVITY` pipeline[16] to extract the relative astrometry and contrast spectrum of the companion relative to the host star. We integrate the GRAVITY spectrum over the Two Micron All Sky Survey (2MASS) K_s-band filter curve to obtain the K_s-band magnitude included in Table 2.

2.2. SPHERE H-band Observations

To extract the properties of WISPIT 2 c, we use the SPHERE *H*-band data observed on the UTC date 2025 March 21 described in R. F. van Capelleveen et al. (2025). In addition, we obtained a new SPHERE/IRDIS *H*-band observation carried out as part of program 115.29HG.002 (PI: C. Ginski) on the UTC date 2025 September 24 with a similar observation setup; see Table 1. This observation includes a dedicated reference observation obtained with the star-hopping technique, alternating approximately every 10 minutes between WISPIT 2 and a reference star. During the science sequence, we obtained 12 full polarimetric cycles, each comprising exposures at the four half-wave plate positions (Q^+, Q^-, U^+, U^-). Each individual exposure had an integration time of 64 s, resulting in a total on-target dual-polarization imaging (DPI) exposure of 51.2 minutes. Over the full science sequence, the pupil-tracking configuration delivered a total parallactic angle rotation of 19.°6. Between science cycles, we recorded 20 reference star frames with an exposure time of 64 s.

In this study, we focus on the total intensity reduction of the SPHERE data and only use the polarized intensity imagery to confirm that there is no strong dust-scattering signal present at

[16] https://gitlab.obspm.fr/mnowak/exogravity

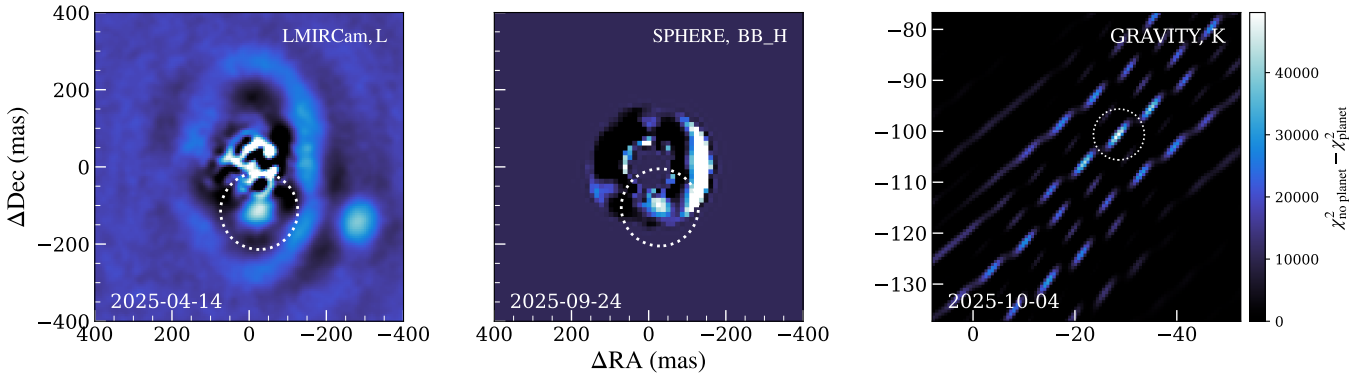

Figure 1. Left: original *L*-band detection of CC 1 in L. M. Close et al. (2025a). Middle: new *H*-band detection of WISPIT 2 c following RDI. We show a confined annulus that was used for optimal stellar signal subtraction. Note that the bright arch on the right side of the annulus is the forward scattering side of the circumstellar disk. Right: detection map of the WISPIT 2 c planet with VLTI/GRAVITY on the night of 2025 October 4. The map shows the periodogram power maps of a point source companion as a function of angular offset from the star, where the companion location corresponds to the strongest peak.

the position of the investigated companion. We extracted the photometry and astrometry of the companion (see Table 2) using negative planet injection combined with a simplex minimization technique, followed by Bayesian inference using Markov Chain Monte Carlo (MCMC; D. J. C. MacKay 2003) with 200 walkers and 10,000 steps, and repeated this method for fake positive injections at positions equidistantly distributed in polar space to extract the systematic errors of the method. All steps are executed with `PynPoint` modules, and the centering precision of 2.5 mas of the star behind the coronagraph, as well as uncertainties in pixel scale, true north correction, and pupil offset, were included in the error budget, analogs to what is described in R. F. van Capelleveen et al. (2025). However, instead of angular differential imaging (ADI) we used reference differential imaging (RDI) with principal component analysis (PCA). Given that the position of WISPIT 2 c is on the inner working angle of the coronagraph, following the recommendation outlined in the SPHERE manual,[17] we apply a correction for the transmission profile of the coronagraph to both the science frames and the reference library. As the observation from the UTC date 2025 March 21 did not have a dedicated reference observation, we leveraged the *H*-band RDI library described in R. F. van Capelleveen et al. (2025). For the observation of the UTC date 2025 September 24, we used the dedicated reference star observations. We found the optimal number of principal components for RDI/PCA to be 12 and 14, respectively. Due to the presence of the bright inner ring, the systematic errors of the method varied with position angle. To account for this, we only included systematic errors similar to those near WISPIT 2 c in our error budget, between a position angle of 335° and 15° (to the north of WISPIT 2) and between a position angle of 120° and 225° (to the south of WISPIT 2). The detection of WISPIT 2 c after PCA/RDI in both observations is included in Figure 1.

3. Nature of the Companion

3.1. Redetection of the Companion with GRAVITY and SPHERE

We redetect the planetary companion WISPIT 2 c with both GRAVITY and SPHERE (see Figure 1), providing independent confirmation of the source previously referred to as CC 1 and reported by L. M. Close et al. (2025a). The detection of embedded, self-luminous protoplanets is a particularly challenging task. In the case of young planets embedded in a protoplanetary disk, it is necessary to distinguish the contribution of the scattered light of the disk from the thermal emission from the planet. Substructures in the disk are usually of comparable scales to the point-spread function (PSF) of 10 m class telescopes. Interferometry is intrinsically sensitive to the coherent emission of point-like sources, which is distinct from the extended background disk signal. The GRAVITY data are key observational evidence for the detection of a new protoplanet in this work.

We followed the approach of GRAVITY Collaboration et al. (2019) and J. J. Wang et al. (2021) to model the coherent flux of the planet $V_{\rm planet}(b,\, t,\, \lambda)$ measured with GRAVITY:

$$V_{\rm planet}(b,\, t,\, \lambda) = C(\lambda) V_{\rm star}(b,\, t,\, \lambda) \exp(i\Phi(b,\, t,\, \lambda)), \quad (1)$$

expressed as a function of the baseline b, time t, and wavelength λ, with $C(\lambda)$ the contrast spectrum estimated from the `ExoGRAVITY` pipeline, as described in M. Nowak et al. (2020), and $V_{\rm star}(\lambda) = F_{\rm star}(\lambda) J_{\rm star}(b,\, t,\, \lambda)$ the coherent flux of the star. The normalized visibility of the star $J_{\rm star}(b,\, t,\, \lambda)$ was calibrated on a reference star HD 180595. We modeled the star spectrum $F_{\rm star}(\lambda)$ using a `BT-Settl-CIFIST` stellar model, as detailed in Appendix A (see Figure 7).

The phase $\Phi(b,\, t,\, \lambda)$ of the planet signal is defined as

$$\Phi(b,\, t,\, \lambda) = -\frac{2\pi}{\lambda}(\Delta{\rm R.A.}u + \Delta{\rm Decl.}v), \quad (2)$$

wherein $(u,\, v)$ are the coordinates in the frequency domain, and $(\Delta$R.A., ΔDecl.) are the sky coordinates of the planet relative to the star. The detection map using this point source model is shown in Figure 1. The detection map shows the periodogram power maps $z(\Delta{\rm R.A.},\, \Delta{\rm Decl.}) = \chi^2_{\rm no\ planet} - \chi^2_{\rm planet}(\Delta{\rm R.A.},\, \Delta{\rm Decl.})$ over the GRAVITY fiber field of view, as described in Equation (B.6) of M. Nowak et al. (2020). The peak of the detection indicates a point-like source, with the side lobes characteristic of the UV coverage of the UT interferometric array. The planet is detected with a signal-to-noise ratio (SNR) > 10 in each of the 12 exposures with GRAVITY. The best fit is achieved at a location of ΔR.A., ΔDecl. = (−29.07 ± 0.024 mas,−101.35 ± 0.038 mas). The presence of a circumplanetary disk (CPD) in addition is discussed in Section 4.2.

[17] https://www.eso.org/sci/facilities/paranal/instruments/sphere/doc.html

3.2. Is it a Bound Planet?

To ascertain the nature of the object labeled CC 1 by L. M. Close et al. (2025a), we follow two independent lines of investigation. We first determine if, with currently available astrometry, we can rule out that the object is a distant background star, and second we test if the GRAVITY spectrum as well as the existing photometry are consistent with an object of planetary nature.

The GRAVITY K-band observation yields a relative astrometry of 105.44 ± 0.04 mas and $196.^{\circ}00 \pm 0.^{\circ}01$. However, the SPHERE K_s-band observation presented in R. F. van Capelleveen et al. (2025) is unusable for astrometry extraction as the source lies too close to the coronagraph, influencing both the photometry and astrometry. With no available published suppression profile of the K_s-band coronagraph, we cannot confidently extract either of these parameters. The L-band astrometry presented in L. M. Close et al. (2025a) is close to the resolution limit for its wavelength and therefore carries large error bars in both separation and position angle and is therefore not sufficiently constraining. At such small separations, we find that, even if the PSF is misaligned by 0.5 of a pixel, this would change the position angle by approximately $2.^{\circ}8$, making the measurement highly sensitive to small systematics. Although the z'-band data by L. M. Close et al. (2025a) provide the longest baseline and smallest error bars, the source appears slightly extended and may include scattered light or CPD emission, which could bias the central position. In addition to these literature values from L. M. Close et al. (2025a), we have extracted the astrometric position of the object from both SPHERE H-band observation epochs, i.e., the epoch taken in 2025 March and originally published in R. F. van Capelleveen et al. (2025), and the new SPHERE H-band observation taken in 2025 September and presented in this study (see Figure 8 in Appendix B for a side-by-side comparison). As we describe in Section 2.2, we applied a total intensity RDI reduction to both of these datasets, which recovers WISPIT 2 c. Conversely to the SPHERE K_s-band epoch, a detailed coronagraphic throughput profile is available for the H-band observations in the SPHERE manual. We thus can reliably extract both astrometry and photometry of WISPIT 2 c. However, because the position of WISPIT 2 c lies near the 50% transmission of the coronagraph, the photometry is sensitive to the accuracy of the throughput correction. Uncertainty in the position of the star behind the coronagraph could lead to small variations in the throughput correction, which has not been propagated into the photometric uncertainty of the companion. While this may result in underestimated H-band magnitude uncertainties, this effect has been partially mitigated by averaging measurements from two independent epochs using two independent reference libraries. Nevertheless, this does not address the possibility of a systematic magnitude offset resulting from over- or under-correction of the throughput if the transmission profile itself is not accurate.

We show all astrometric measurements in Figure 2. In the same figure, we also illustrate the expected location of a nonmoving background source. Due to the short time baseline, the relative position angle of a gravitationally bound, comoving source and a background object show considerable overlap. However, we do expect a strong change in separation for a background object that should not be present for a comoving source. We find that the position angle from the literature data from L. M. Close et al. (2025a) in combination with our new GRAVITY observation appears to rule out a background object, while the SPHERE H-band epochs are consistent with both a background object and a comoving bound planet. For separation, the GRAVITY and SPHERE H-band data as well as the literature z'-band data rule out a background object, while the L-band data uncertainties are too large to distinguish between both scenarios. Given that the data points with the smallest uncertainties appear to rule out a nonmoving background object, both in position angle and separation, we conclude that WISPIT 2 c is a bound object in the system.

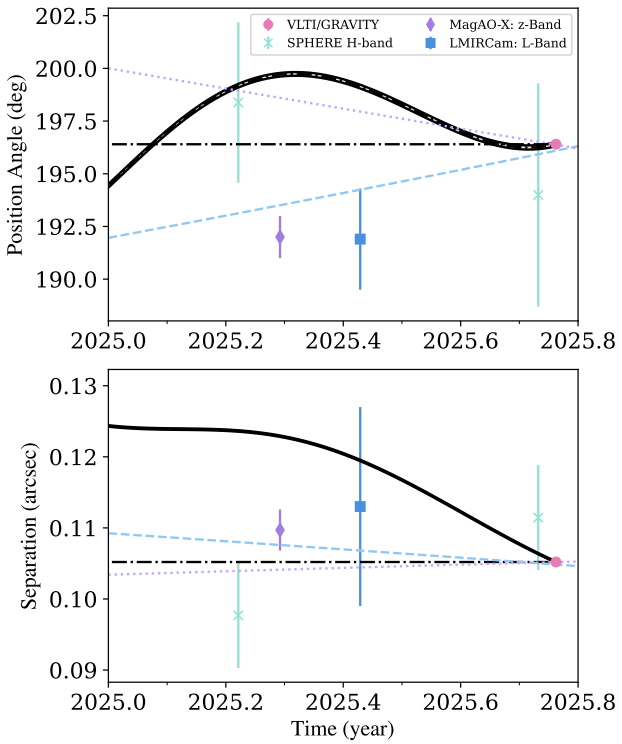

Figure 2. Relative astrometry of WISPIT 2c to the primary star over time. We give the separation and position angle (measured from north over east). The purple dashed line indicates plausible orbital motion for a prograde orbit, while the blue dashed line indicates retrograde motion. Both orbits are in the plane of the circumstellar disk. The solid curved line indicates the expected behavior for a distant background object, while the black dashed line represents no relative change of motion in relation to the host star.

However, we note that the object shows a measurable change in position angle and separation compared to the GRAVITY measurement. This suggests that the object exhibits genuine orbital motion. Assuming the planet lies in the disk plane (inclination fixed at 45°), we estimate the possible orbital solutions with orbitize! (S. Blunt et al. 2020) using an emcee MCMC sampler (D. Foreman-Mackey et al. 2013). Based on the current astrometry, we can explain the tentative change with Keplerian orbits, albeit with some inconsistency between the SPHERE H-band and literature z'- and L-band data points. While the former indicate orbital motion in the same direction as the outer planet WISPIT 2b, as reported in R. F. van Capelleveen et al. (2025), the latter exhibit a change in position angle, which would put the orbit of 2 c in retrograde relative to 2b. We illustrate both prograde and retrograde solutions in our proper motion analysis in Figure 2. We note that a retrograde orbit would be extremely unusual and, given the potential biases in the z'-band centroid

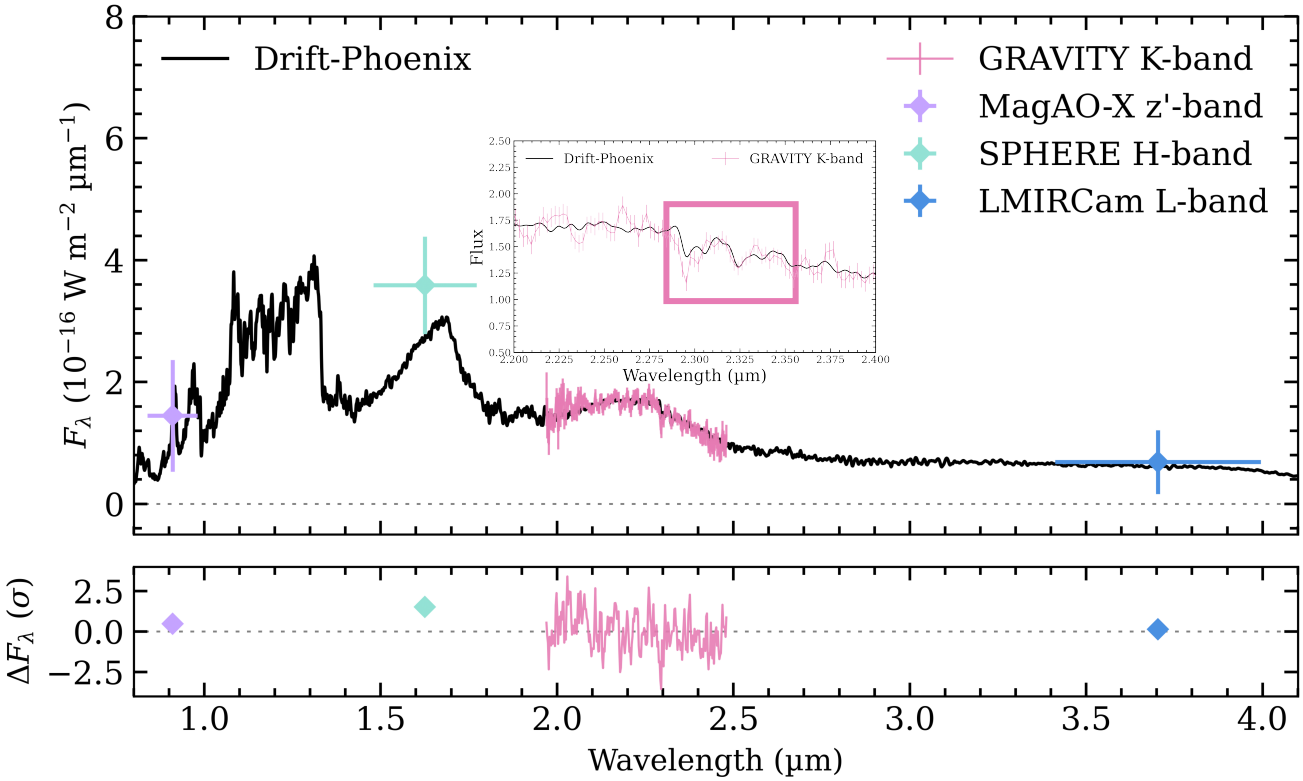

Figure 3. `Drift-Phoenix` spectral model overlaid with the *K*-band spectrum obtained with VLTI/GRAVITY, *H*-band VLT/SPHERE, z'-band MagAO-X, and *L*-band LBTI/LMIRCam photometry of WISPIT 2 c. The modeled spectrum is based on the max likelihood fitting of temperature and radius. The figure also contains a zoomed-in region of 2.2–2.4 μm to highlight the CO absorption band heads, marked by the pink box.

and the limited precision of the *L*-band measurement, we find the prograde orbit indicated by the SPHERE *H*-band data to be the more likely scenario. Additional high-precision astrometry will be required to confirm the orbital direction of WISPIT 2 c.

With a distant background object ruled out by the astrometric analysis, we inspected the *K*-band spectrum of WISPIT 2 c. Figure 3 shows CO absorption in the GRAVITY *K*-band spectrum at 2.2935 μm and a positive slope from 2.15–2.25 μm, both well-established signatures of young, low-gravity substellar objects (J. Patience et al. 2012; K. N. Allers & M. C. Liu 2013). Such CO absorption is expected to remain prominent in the atmospheres of young giant planets but is not produced at detectable levels in stellar photospheres beyond temperatures of ~5300 K (M. Cesetti et al. 2013). The photometric measurement in the *H* band may follow the characteristic triangular continuum shape that arises from deep H_2O absorption on both sides of the 1.65 μm peak (K. N. Allers & M. C. Liu 2013), though our current data cannot confirm this as we cover this wavelength regime only with a single photometric point.

Taken together, both the astrometry as well as the spectroscopic data strongly indicate that CC 1 is indeed a second planet in the system, which we will now refer to as WISPIT 2 c.

3.3. Temperature and Mass of WISPIT 2c

To assess the atmospheric properties of WISPIT 2 c, we employed the spectral and photometric tool `species` (T. Stolker et al. 2020b), which is commonly used for the analysis of directly imaged planets and brown dwarfs. We performed an atmospheric parameter inference by sampling self-consistent atmospheric model grids with the nested sampler `dynesty` (J. S. Speagle 2020) fitting the `Drift-Phoenix` (P. H. Hauschildt & E. Baron 1999; E. Baron et al. 2003; P. Woitke & C. Helling 2003, 2004; C. Helling & P. Woitke 2006; C. Helling et al. 2008a, 2008b; S. Witte et al. 2009, 2011) model. We furthermore also explore several additional models, the results of which we describe in Appendix D.

`Drift-Phoenix` is designed for the dust-rich atmospheres we expect of young embedded planets, and it includes detailed cloud microphysics (A. S. Rajpurohit et al. 2012). For the atmosphere constraint, we consider the z'- and *L*-band photometric points by L. M. Close et al. (2025a) as well as our new SPHERE *H*-band photometric measurement and GRAVITY *K*-band spectrum. We discuss in Appendix D how the recovered parameters are influenced if we use various subsets of these data points. As we are not sensitive to variations in log *g* (see Figure 10 in Appendix D), varying log *g* between 3 and 5 does not significantly modify the inferred atmospheric parameters. Taking an average of the available log *g* values for young (<50 Myr) gas giants (J. Schneider et al. 2011) returns an average log *g* of ~3.9, which we take as a fixed value. As WISPIT 2 is a solar-type star, we fix [Fe/H] at 0.0; similar to log *g*, we are not sensitive to changes in metallicity (see Figure 11 in Appendix D).

Employing the `Drift-Phoenix` model, we derive max likelihood planet parameters of $T_{\rm eff} = 1754 \pm 16$ K and $R = 1.78 \pm 0.03\,R_{\rm Jup}$, where the errors are purely statistical (see Figure 12 in Appendix D for model distributions). Since the

Table 3
Ranges of Physical Parameters of WISPIT 2 c Based on the Atmospheric Model Fitting from the Models Presented in Appendix D, Separated Based on High- and Low-temperature Families

Planet Parameters	High T	Low T
$T_{\rm eff}$ K	**2300–2600**	**1500–1750**
log g	3.9[a]	3.9
[Fe/H]	**0.0**	**0.0**
$R_{\rm p}/R_{\rm Jup}$	**0.91–1.07**	**1.78–2.20**
$\log L_{\rm p}/L_{\odot}$	**(–3.47)-(–3.53)**	**(–3.55)-(–3.63)**
$M_{\rm p}/M_{\rm Jup}$	**3–14**	**10–16**
$M_{\rm p}/M_{\rm Jup}$	**8–**12[b]	

Notes. The ranges are based on the highest and lowest most likelihood values of each model, and we do not report statistical errors as they are negligible.
[a] Note the exception of the `BT-Dusty` model, where log g is 4.5.
[b] Mass range derived from luminosity–mass isochrones.

pure statistical uncertainties are clearly underestimating the possible temperature and radius range for the planet, we consider the full set of explored models in Appendix D to obtain a temperature range of 1500–2600 K and a radius range of 0.91–2.20 $R_{\rm Jup}$.

The distribution of temperatures appears bimodal; hence, we separate the models into high- and low-temperature families, and more specific ranges can be seen in Table 3. We note, however, that the ranges produced by the `BT-Dusty`, `Sonora-Bobcat`, `BT-Settl`, and `ATMO` models appear unphysical; as such, a young object is expected to have an inflated radius (see, e.g., D. S. Spiegel & A. Burrows 2012). Given that the `Drift-Phoenix` model is a closer fit to our K-band spectrum with minimal residuals and produces more reasonable temperature and radius values, we consider these values more likely. This conclusion is further strengthened by comparison of the K_s-band magnitude and $H - K_s$ color against evolutionary isochrones (see the discussion below), which imply inflated radii larger than 1.6 $R_{\rm Jup}$.

We show the best-fit `Drift-Phoenix` model and overlay our extracted GRAVITY K-band spectrum and z'-, H-, and L-band photometry in Figure 3. The model spectrum closely follows our extracted K-band spectrum, with a characteristic CO absorption at 2.2935 μm and overtones between 2.33 and 2.36 μm, highlighted in the inset of Figure 3. The best-fit results for the alternative models that we explored are shown in Figure 13 in Appendix D. The `BT-Dusty`, `Sonora-Bobcat`, `BT-Settl`, and `ATMO` models converge toward high-temperature (∼2300–2600 K) solutions that imply unphysically small radii (0.91–1.07 $R_{\rm Jup}$), inconsistent with expectations for a young, inflated object. Given that our two best-fitting models, `Drift-Phoenix` and `ExoRem`, i.e., the models with the smallest residuals, both include cloud physics, this may suggest that WISPIT 2 c possesses a dusty atmosphere; given that the planet is still young, this is expected due to its low surface gravity (M. S. Marley & S. Sengupta 2011; B. Charnay et al. 2018).

In addition to our model grid exploration, we compare the GRAVITY K-band spectrum of WISPIT 2 c with the spectra of PDS 70b and HR8799 e, which are taken from the ExoGRAVITY K-band spectral library of gas giants and brown dwarfs presented in J. Kammerer et al. (2025). These two objects were selected based on their similar absolute luminosity compared to WISPIT 2 c. The resulting comparative spectra are shown in

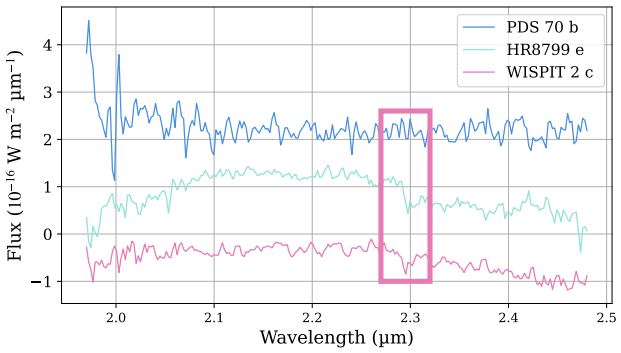

Figure 4. K-band GRAVITY spectra of PDS 70b, HR8799 e (J. Kammerer et al. 2025), and WISPIT 2 c. Offsets have been applied along the y-axis The CO feature (highlighted by the pink box) can be clearly seen in HR8799 and WISPIT 2 c, but is lacking in PDS 70b.

Figure 4. We note that the continuum shape and depth of CO absorption features of WISPIT 2 c and HR8799 e are overall similar. While HR8799 e is found to be slightly colder than WISPIT 2 c (1100–1400 K; E. Nasedkin et al. 2024), it confirms that our spectrum is consistent with a young gas giant planet. Conversely, the spectrum of PDS 70b, a planet still located within its birth disk, appears almost flat with no strong CO feature. J. J. Wang et al. (2021) discuss that the spectrum is most likely explained by a planetary atmosphere with significant amounts of dust, the nature of which is uncertain. The difference in spectrum between PDS 70b and WISPIT 2 c may then indicate that the former is still strongly embedded, while this is not true for the latter.

Using the luminosity derived from our radius and temperature range, we estimate the mass of WISPIT 2 c by comparison to evolutionary model isochrones. To determine the sensitivity of our mass estimate to assumptions of age and evolutionary models, we computed isochrones for WISPIT 2 c using a range of representative ages and atmosphere grids. In Figure 5, we show isochrones at 3.8, 5.1, and 7.5 Myr (the system age of 5.1 Myr and its associated errors reported in R. F. van Capelleveen et al. 2025). For each age, we compare the predicted luminosity–mass relations with our measured luminosity, including its uncertainty range, taken from our posterior samples. Across this age span, we infer a corresponding mass range of approximately 8–12 $M_{\rm Jup}$, consistent with the values previously reported for CC 1 by L. M. Close et al. (2025a) of 8–10 $M_{\rm Jup}$. We tested how robust this estimate is against the usage of different model isochrones and found a mass range of roughly 9–11 $M_{\rm Jup}$, i.e., smaller than the range given by the uncertainty of the system age. Based on these mass ranges, it appears likely that WISPIT 2 c sits comfortably in a range of 8–12 $M_{\rm Jup}$. However, we note that our atmospheric grid models infer a broader range of masses of 3–16 $M_{\rm Jup}$. Since mass is not a fitted parameter in these models but is instead derived from the fixed log g and inferred radius, we do not consider these to be robust mass estimates as our data are not sensitive to small changes in log g, as mentioned previously.

In addition to our spectral analysis, the photometry of WISPIT 2 c is shown in a color–magnitude diagram in Figure 6, along with that of WISPIT 2b and other known planets with available H- and K_s-band magnitudes. Comparison against 5.1 Myr `Sonora-Bobcat` (M. S. Marley et al. 2021) and `Sonora-Diamondback` (C. V. Morley et al. 2024) isochrone tracks confirm that WISPIT 2 c is a planetary

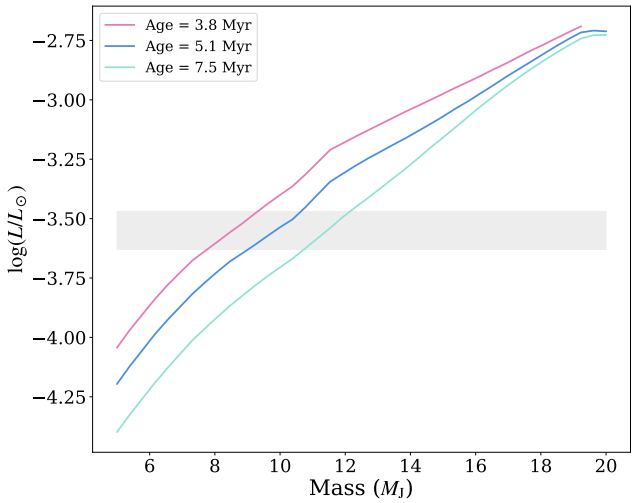

Figure 5. `Sonora-Diamondback` luminosity–mass isochrones at varying ages; measured luminosities from the atmospheric model fitting are shown by the gray shaded region.

mass companion and that the $H - K_s 1\sigma$ upper bound is consistent with a cloudy model, in agreement with the best-fit atmosphere models to the combined spectrum and photometry. We note that the lower temperature and inflated radius are also preferred from comparison against these evolutionary isochrones.

4. Discussion

4.1. Comparison with PDS 70

The young T Tauri star PDS 70 (J. Gregorio-Hetem et al. 1992) once acted as a lone candle in the dark for early planet formation studies, owing to its two confirmed planets, PDS 70b (M. Keppler et al. 2018) and PDS 70 c (S. Y. Haffert et al. 2019). The confirmation of two planets in the young WISPIT 2 system now provides a valuable second comparison point, helping to narrow the observational gap in our understanding of how giant planets convene within their natal disks. Although the sample of directly imaged, still embedded protoplanets remains too small for robust statistical analyses, it is still informative to compare the orbital architectures of WISPIT 2 and PDS 70.

PDS 70 exhibits a well-defined inner cavity, host to two planets, measuring roughly 70 au (R. Dong et al. 2012; J. Hashimoto et al. 2012, 2015; M. Keppler et al. 2019), similar to that of WISPIT 2's prominent 60 au gap, containing one planet, with a second planet sitting beyond the innermost ring. Both systems show strong signs of being shaped by their respective planets. Despite the more extended disk in WISPIT 2, the confirmed planets in both systems occupy a broadly similar radial regime, approximately 57 and 14 au for WISPIT 2b and c, and 21 and 35 au for PDS 70b and c (S. Y. Haffert et al. 2019). The lack of a dust ring between the planets in PDS 70 is likely due to the close separation between its respective planets. These planets likely would have accreted material from both sides of the ring early in their formation stages, thus depleting the dust ring and forming the large cavity that now harbors these planets, while the planets in WISPIT 2 are at a much larger separation and therefore are unable to efficiently clear the material between them, allowing the dust ring to remain intact. Recent astrometric fits by D. Trevascus et al.

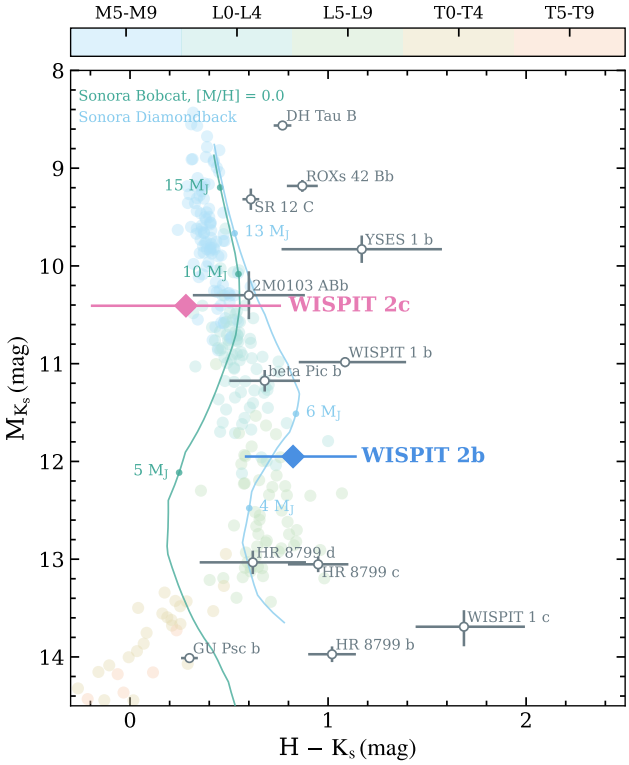

Figure 6. Color–magnitude diagram of the WISPIT 2 system, along with confirmed planetary companions and field brown dwarfs of various spectral types. The teal and cyan tracks show 5.1 Myr `Sonora-Bobcat` (cloud free) and `Sonora-Diamondback` (hybrid clouds; sedimentation efficiency $f_{\rm sed} = 2$) evolutionary isochrones, respectively.

(2025) place upper mass limits of 4.9 and 13.6 $M_{\rm Jup}$ for PDS 70b and c, respectively, comparable to the masses of WISPIT 2b and c. These broadly similar radial and mass ranges may imply the existence of a "Goldilocks zone" for early giant planet formation, where conditions in both systems appear to be conducive to generating giant multiplanet architectures. It is likely that the planets in both WISPIT 2 and PDS 70 formed in situ (see G. Perotti et al. 2023; R. F. van Capelleveen et al. 2025), implying their current locations trace the environments that supported their formation rather than the endpoints of substantial inward or outward migration.

4.2. Nondetection of Hα and CPD

Despite its larger mass compared to the previously detected outer planet WISPIT 2b, there was no significant Hα emission detected at the position of WISPIT 2 c (L. M. Close et al. 2025a). Given that accretion generally scales with mass (see, e.g., B. Ercolano et al. 2014; C. F. Manara et al. 2023), this indicates that either the accretion on the object is highly variable or that the object is veiled by circumplanetary dust, which effectively blocks the optical wavelength emission. As we only have a single epoch of Hα imaging of the system to date, we are unable to verify if the accretion signatures of the planet might be variable. However, from large spectroscopic surveys, we know this commonly to be the case for young stars (e.g., C. F. Manara et al. 2021). Given that the transport mechanisms within the disk for accretion onto the central star or a surrounding planet are similar, it is reasonable to assume that this is indeed also the case for the accretion activity of the planet. This indeed has been recently confirmed for the planets

in the PDS 70 system (L. M. Close et al. 2025b; Y. Zhou et al. 2025).

On the other hand, L. M. Close et al. (2025a) point out that the z'-band measurement appears to be tentatively extended, consistent with a CPD signal within the Hill radius of a massive planet. Conversely, our preliminary GRAVITY observation rules out the presence of a compact CPD at scales of ∼0.25 au. This may indicate that, if a CPD is indeed present, then the dust grain sizes within the disk are on a submicron scale, so that they efficiently scatter light in the optical z' band but do not significantly contribute to the signal in the K- band. Alternatively, this could indicate that there is some larger-scale dusty envelope present at the position of WISPIT 2 c, in fact very similar to what has been observed for PDS 70 c (T. Stolker et al. 2020a). This envelope could then be detected in the z' -band but resolved out by the interferometric GRAVITY observation. The presence of such an envelope could then also explain the nondetection at the Hα wavelength.

4.3. Planet Orbital Eccentricity and Multiplicity

The confirmation of a second planet in the WISPIT 2 system aligns with expectations based on its dynamical behavior. The previously detected planet in the system, WISPIT 2b, exhibits an extremely low eccentricity ($e \leqslant 0.2$), consistent with trends observed in multiplanet systems. Studies by J.-W. Xie et al. (2016) found that, from a sample of Kepler planets, the average eccentricity for single planets is approximately 0.3, while systems with multiple planets tend to have significantly lower average eccentricities of 0.04. Similarly, M. A. Limbach & E. L. Turner (2015) reported a strong inverse correlation between planet multiplicity and orbital eccentricity. Follow-up observations will be key to constrain the orbits of both planets in the system to establish solid links between orbital architecture and planet multiplicity.

5. Conclusions

Through combined photometric and spectroscopic analysis, we confirm the presence of an additional planetary mass companion in the WISPIT 2 system. The CO band head detected in the GRAVITY K-band spectrum provides strong evidence for a planetary object, which is twice as massive as WISPIT 2b and significantly closer to the host star, with a mass range of 8–12 $M_{\rm Jup}$ and a radial separation of 14 au. While WISPIT 2b showed strong signs of Hα emission, there is an absence of significantly detectable Hα emission from WISPIT 2 c, which may indicate strong variability or dust veiling. With current available astrometry, the motion of the planet appears inconsistent with that of a distant background object, but further high-precision astrometric observations are needed to constrain its orbital motion. With this new detection, WISPIT 2 becomes only the second system (after PDS 70) to host multiple directly imaged young giant planets in formation, making it a prime target for follow-up observations with the upcoming Extremely Large Telescope (ELT). This offers a rare opportunity to probe how early system architectures emerge. Although still speculative, the comparable orbital separations in both systems may hint at a "Goldilocks zone" for giant planet formation in young disks. While the available data remain limited, these results bring us one step closer to making direct connections between the initial conditions of planet formation and the final architectures of planetary systems.

Acknowledgments

The authors would like to thank an anonymous referee for comments that significantly improved the clarity of the Letter. C. L. would like to acknowledge support from the COST Action CA22133 PLANETS. The authors would like to thank Ilya Ilyin for fruitful discussion of their results. We thank the Fundação para a Ciência e Tecnologia (FCT), Portugal, for the financial support to the Center for Astrophysics and Gravitation (CENTRA/IST/ULisboa) through grant No. UID/PRR/00099/2025 (https://doi.org/10.54499/UID/PRR/00099/2025) and grant No. UID/00099/2025 (https://doi.org/10.54499/UID/00099/2025). S.F.H. and C.S. acknowledge support through UK Research and Innovation (UKRI) under the UK government's Horizon Europe Funding Guarantee (EP/Z533920/1, selected in the 2023 ERC Advanced grant round). S.F.H. and J.-B.L. acknowledge support through an STFC Small Award (ST/Y001656/1). Part of this research was carried out in part at the Jet Propulsion Laboratory, California Institute of Technology, under a contract with the National Aeronautics and Space Administration (80NM0018D0004). This research is based on observations collected at the European Southern Observatory under ESO programmes 114.27EK.002, 115.29HG.001, and 115.29HG.002.

Appendix A
Flux Calibration of the GRAVITY Data

The spectral energy distribution (SED) from the star was obtained by fitting the photometry point from GAIA DR3 (Gaia Collaboration et al. 2023) and 2MASS (R. M. Cutri et al. 2003), used in R. F. van Capelleveen et al. (2025). The absolute flux of the star was obtained with a synthetic spectrum from the `species`[18] package, using a `BT-Settl-CIFIST` stellar model. The result of the fit of the SED is shown in Figure 7. Finally, the absolute flux of the planet spectrum is obtained by multiplying the contrast spectrum extracted from the `ExoGRAVITY` pipeline with the synthetic spectrum of the star.

[18] https://species.readthedocs.io/

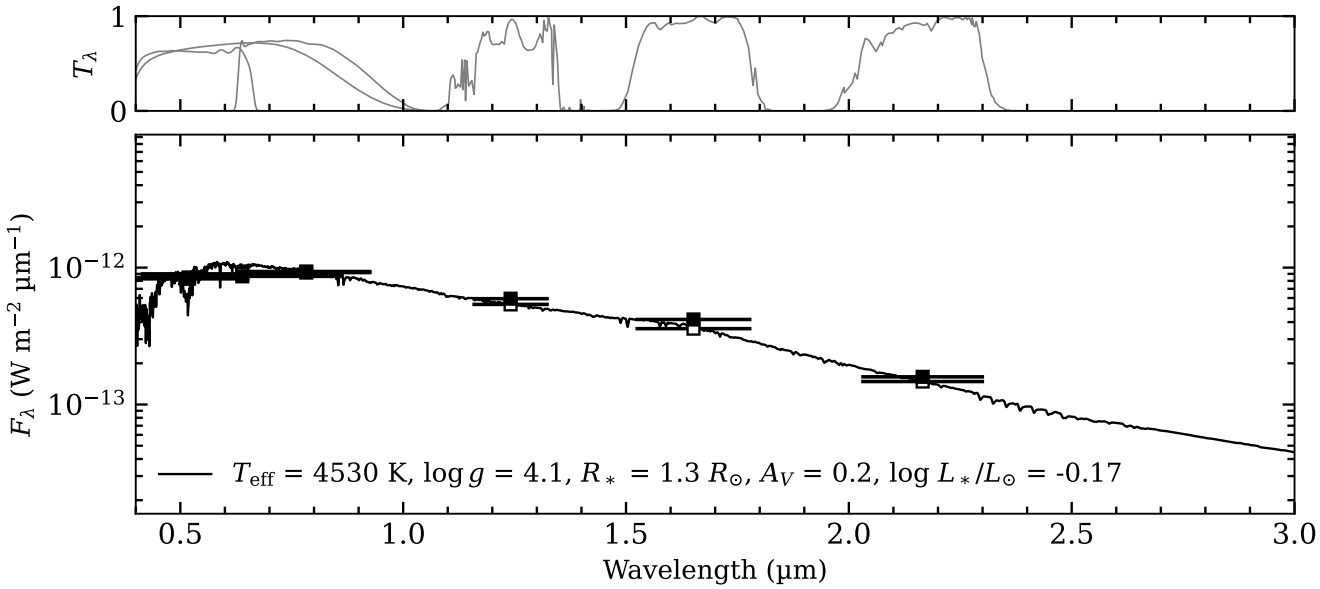

Figure 7. Fitted stellar SED of WISPIT 2 used for the absolute flux calibration of the GRAVITY data.

Appendix B
Comparison of the Two SPHERE Observation Epochs

We show the RDI reduced (total intensity) SPHERE observations taken in 2025 March and September in Figure 8. Both were taken with similar instrument settings and in the *H*-band filter. The main difference between the two epochs is the applied reference star data. While for the 2025 September epoch a dedicated reference star was observed in "star-hopping mode," i.e., interleaved with the science observation, this was not the case for the 2025 March data. For this dataset, instead a reference library was utilized. Both observation epochs recover the companion at high significance.

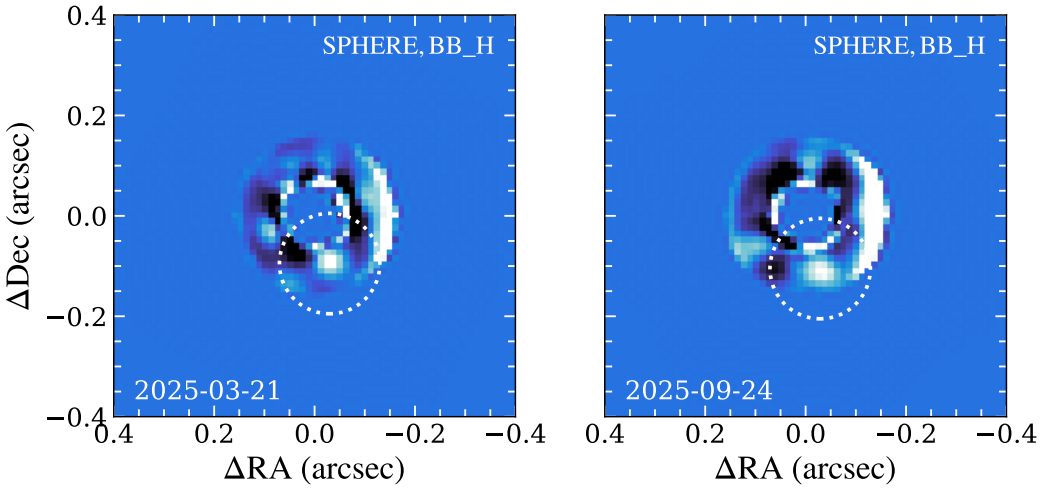

Figure 8. SPHERE *H*-band observations of the new planet WISPIT 2c. Both observation epochs clearly recover the planet (marked with the dotted circle). A mask is applied to exclude the majority of the disk signal from the extraction and prevent oversubtraction. Both images utilize a linear color map.

Appendix C
Red, Green, and Blue Image of the WISPIT 2 System

In Figure 9, we show a red, green, and blue (RGB) image of the WISPIT 2 system using existing literature data as well as our new SPHERE *H*-band observations. The red channel in the image is comprised of the ADI-treated *L*-band data from L. M. Close et al. (2025a), while the green channel uses the RDI-treated SPHERE *K*-band data first presented in R. F. van Capelleveen et al. (2025). The blue channel uses our newly obtained SPHERE *H*-band data. Here, we use a composite of the RDI-treated annulus confined data that recovers the planet WISPIT 2 c and which is shown in Figure 1, and a polarization image showing the disk-scattered light created from the same dataset (but not sensitive to the planet). Each channel was normalized such that the disk has a similar brightness toward its forward scattering peak. The brightness of each channel is scaled with the square root of the pixel values, which provides good contrast between planet signal and noise. We note that this image should be primarily considered for illustration of the system architecture and is not meant for an accurate color analysis of the disk or the planet signal.

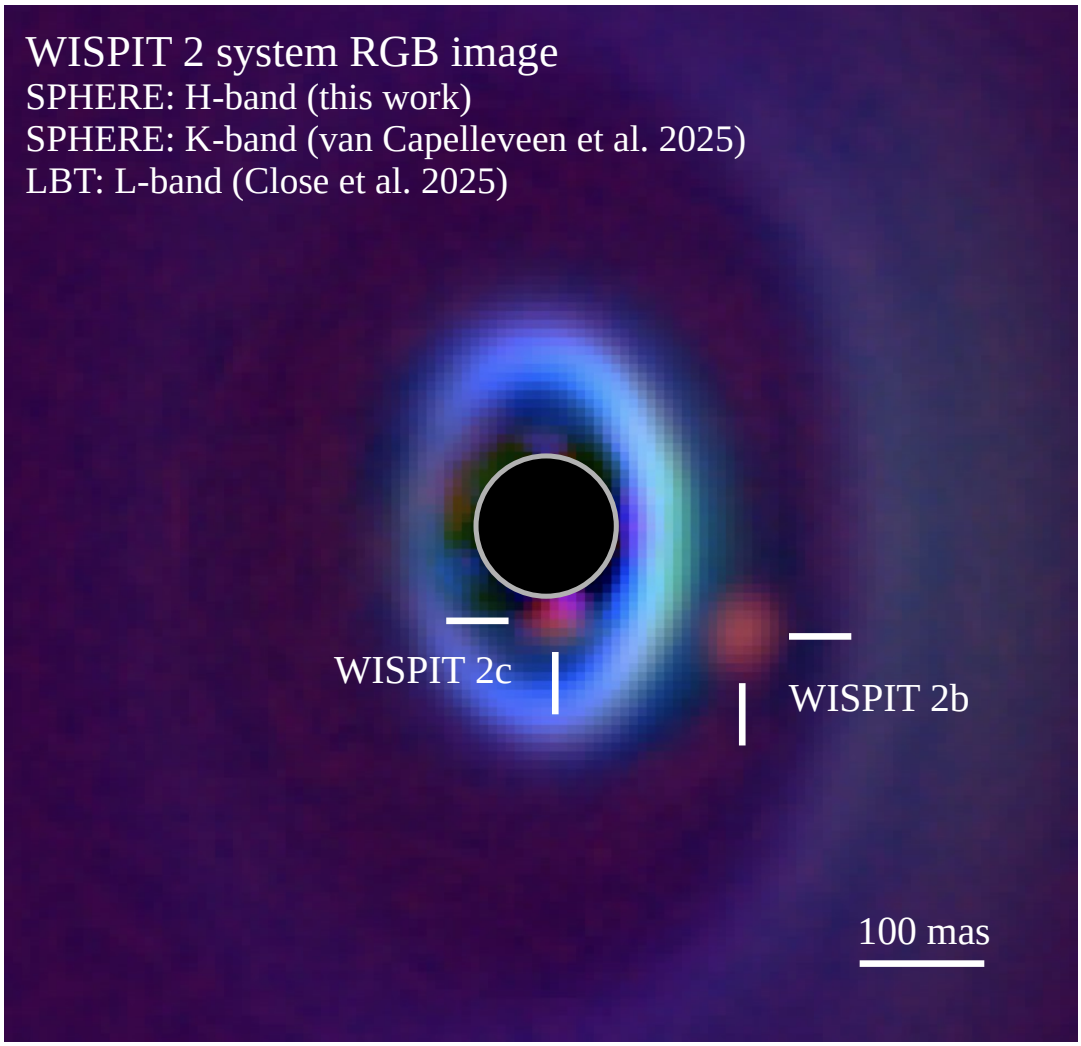

Figure 9. RGB image of WISPIT 2 using the existing *L*- and *K*-band data by L. M. Close et al. (2025a) and R. F. van Capelleveen et al. (2025), as well as our new *H*-band data. We mark the positions of the known planet WISPIT 2b as well as the new inner planet WISPIT 2 c.

Appendix D
Full Nested Sampling Inference of Planet Atmosphere Parameters

We performed a full atmospheric parameter inference of WISPIT 2 c using the `species` tool (T. Stolker et al. 2020b). The analysis combines both the medium resolution *K*-band spectrum extracted from the GRAVITY observations, using the standard deviation errors of the spectrum, and the z'-, *H*-, and *L*-band photometry.

We use the `Drift-Phoenix` (P. H. Hauschildt & E. Baron 1999; E. Baron et al. 2003; P. Woitke & C. Helling 2003, 2004; C. Helling & P. Woitke 2006; C. Helling et al. 2008a, 2008b; S. Witte et al. 2009, 2011), `Sonora-Diamondback` (C. V. Morley et al. 2024), `ExoRem` (J.-L. Baudino et al. 2015; B. Charnay et al. 2018), `BT-Dusty` (F. Allard et al. 2012), `Sonora-Bobcat` (M. S. Marley et al. 2021), `BT-Settl` (F. Allard 2014), and `ATMO` (M. W. Phillips et al. 2020) models to explore a variety of physical properties for the planetary atmosphere. The model grids cover a wavelength range of 0.5–10 μm with a spectral resolution of 500 (consistent with that of the GRAVITY instrument) and 1000 live points. We adopted uniform priors with reasonable ranges of 1500–3000 K and 0.5–3.5 R_J. We fix the surface gravity log g at 3.9 for all models (the average of reported values for young gas giants), with the exception of `BT-Dusty`, where it was fixed at 4.5, as this is the minimum value accepted by the model grid.

We do not attempt to constrain these values as the continuum shape is only marginally influenced by log g, and we do not resolve any individual spectral lines that would be strongly influenced (see Figure 10). Because the GRAVITY spectrum has a moderate spectral resolution, the *K*-band spectrum is not sensitive enough to the depth of lines to determine the abundances of individual elements (S. Rukdee 2024; see Figure 11). For this reason, we fix the metallicity at 0.0, assuming a solar value. The resulting posterior distributions for out best-fit `Drift-Phoenix` model are shown in Figure 12. Additional analysis determined that the atmospheric constraints are dominated by the *K*-band spectrum. Starting from the *K*-band spectrum, we ran our sampler to extract the planet parameters and added *L*, *H*, and z', in that order. We find this produces only a very minimal change in temperature, on the order of tens of kelvin, letting us include all photometric points in the final fits. We show in Figure 13 a comparison of our test models. As the fits with the smallest residuals appear to be `Drift-Phoenix` and `ExoRem`, this may imply a cloudy atmosphere, although we do note that both `BT-Settl` and `Sonora-Diamondback` also employ cloud physics but are not ideal fits to the data.

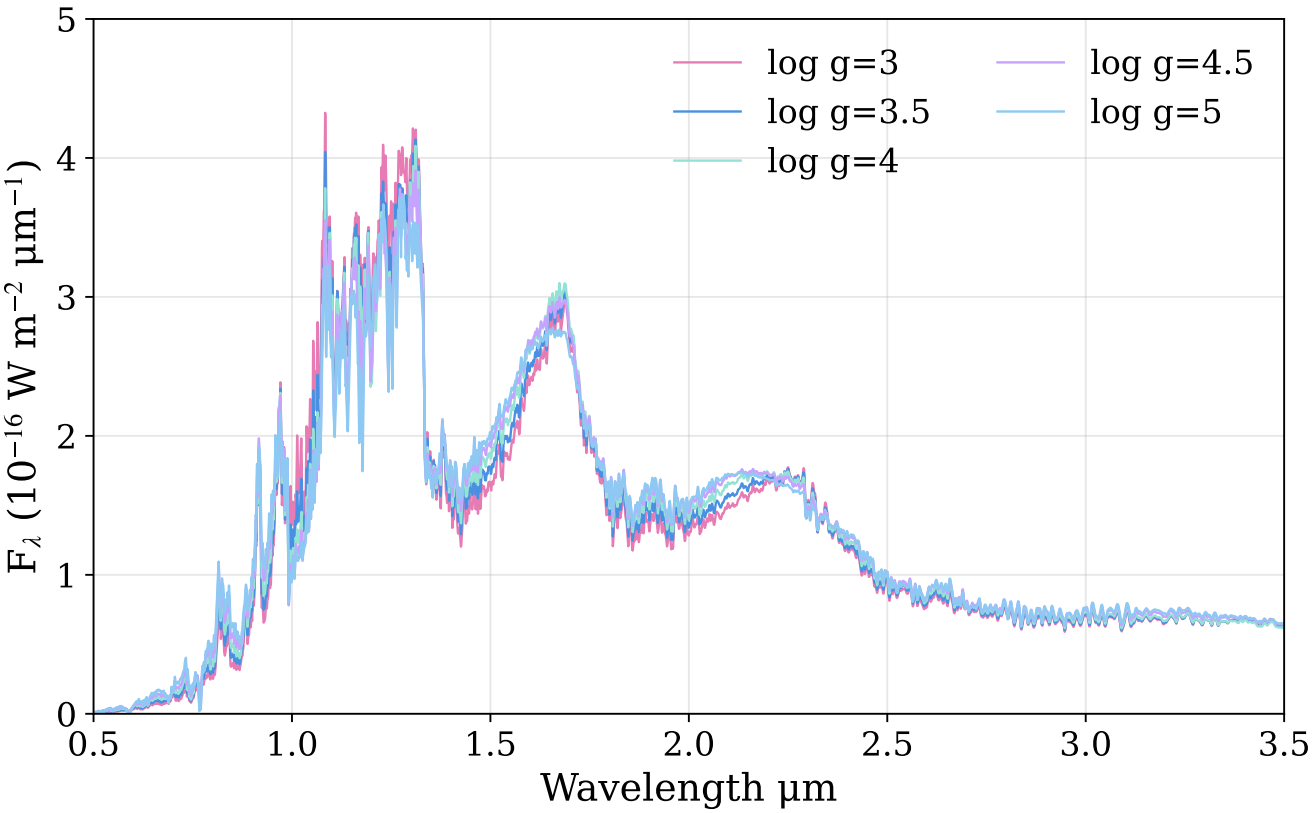

Figure 10. `Drift-Phoenix` model spectrum of the WISPIT 2 c atmosphere with varying log g, at a fixed temperature of 1750 K and a radius of 1.78 $R_{\rm Jup}$.

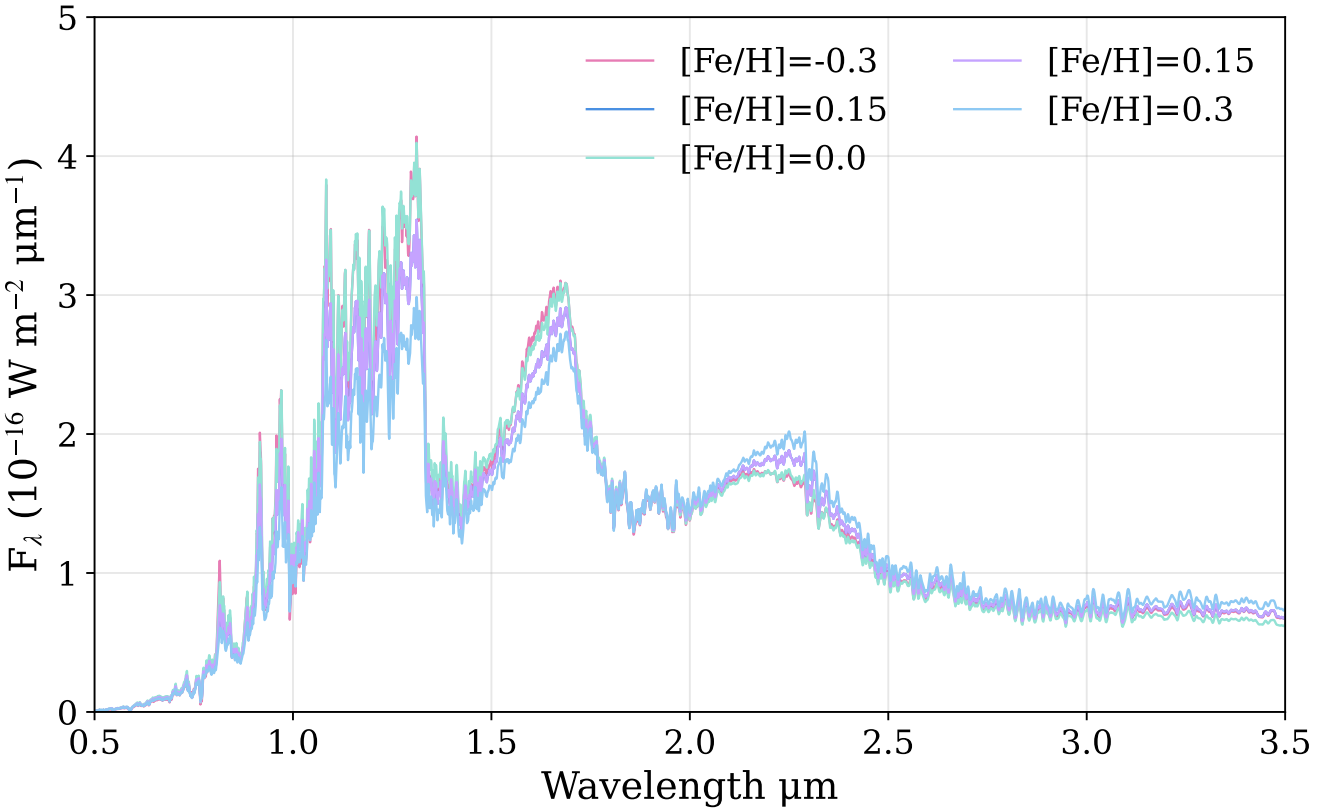

Figure 11. `Drift-Phoenix` model spectrum of the WISPIT 2 c atmosphere with varying metallicity, at a fixed temperature of 1750 K and a radius of 1.78 $R_{\rm Jup}$.

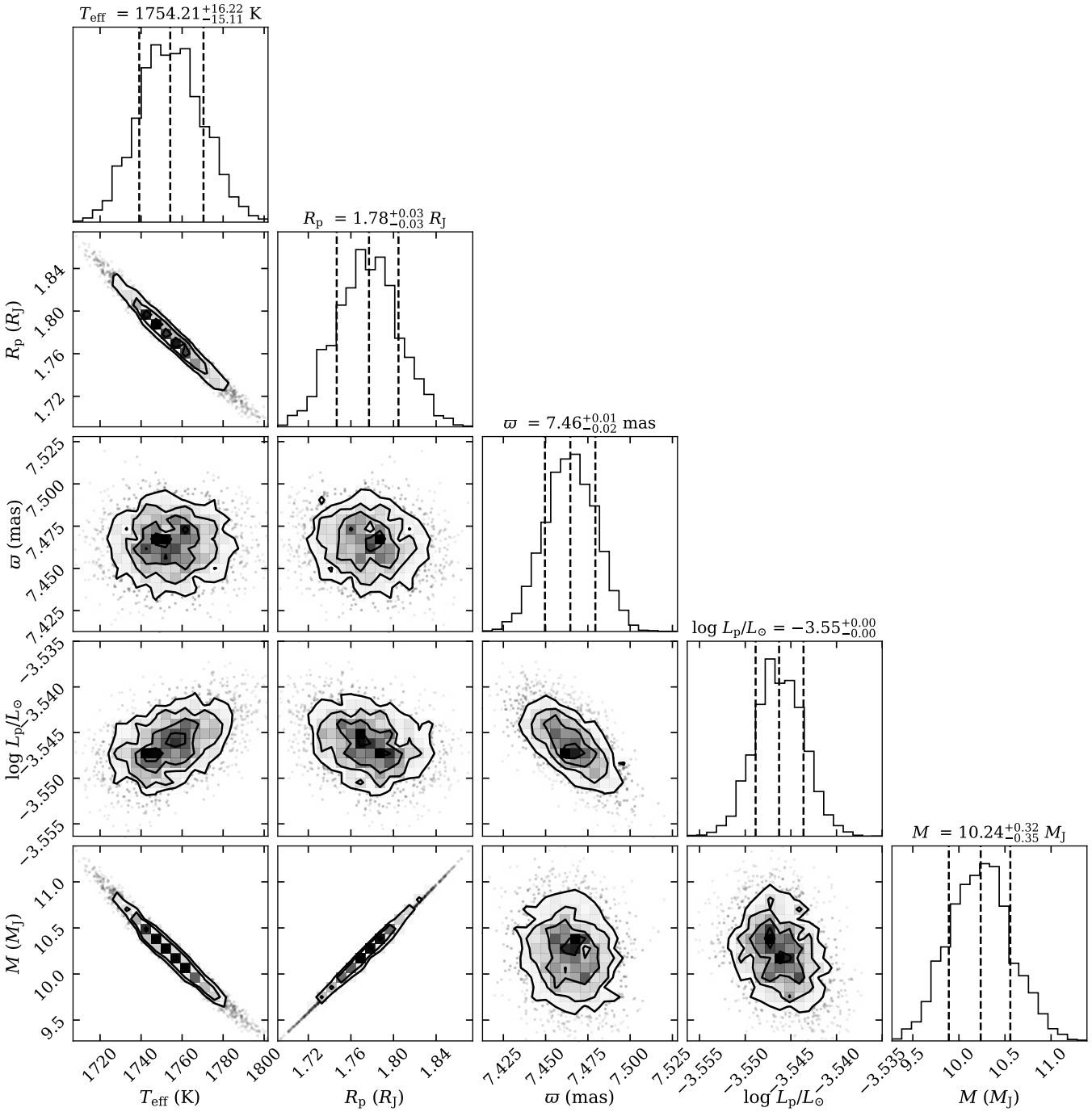

Figure 12. Posterior distributions for WISPIT 2 c from the nested sampling using `Drift-Phoenix`, with median values shown and $\pm1\sigma$.

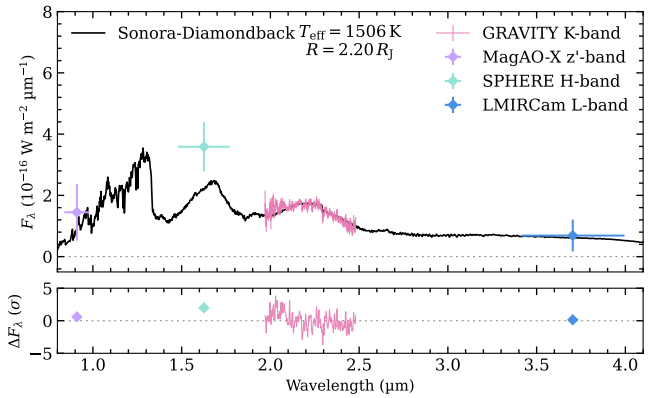

(a) `Sonora-Diamondback` **best fit spectrum with inferred planet temperature and radius.**

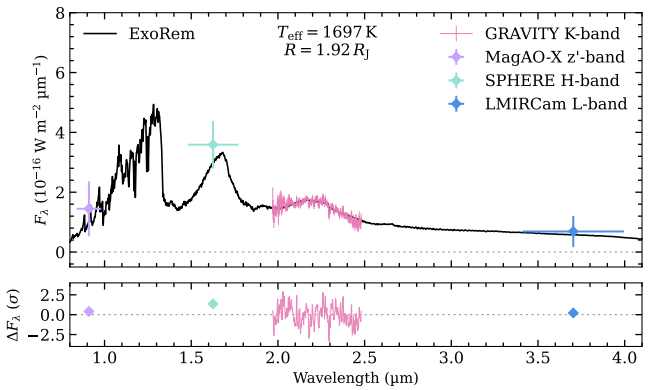

(b) `ExoRem` **best fit spectrum with inferred planet temperature and radius.**

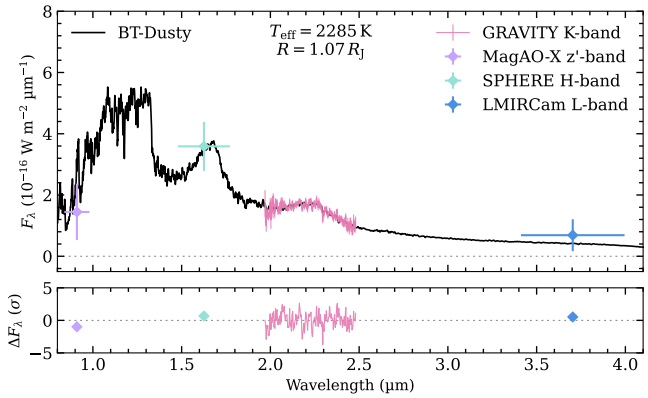

(c) `BT-Dusty` **best fit spectrum with inferred planet temperature and radius.**

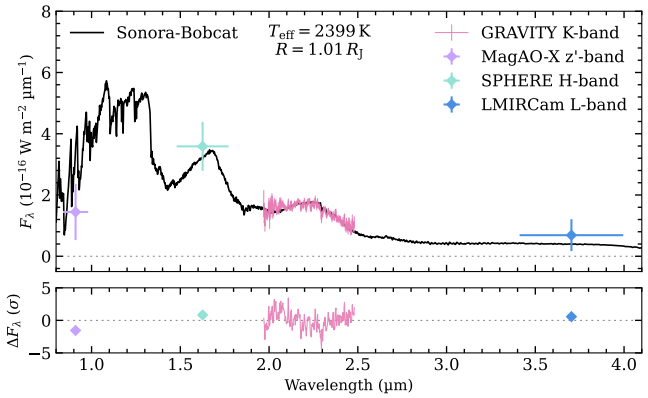

(d) `Sonora-Bobcat` **best fit spectrum with inferred planet temperature and radius.**

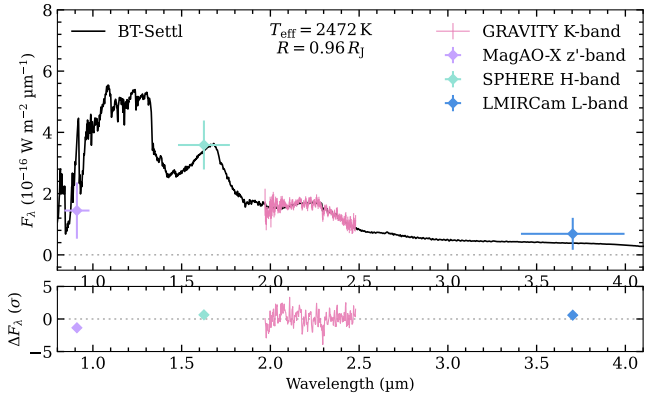

(e) `BT-Settl` **best fit spectrum with inferred planet temperature and radius.**

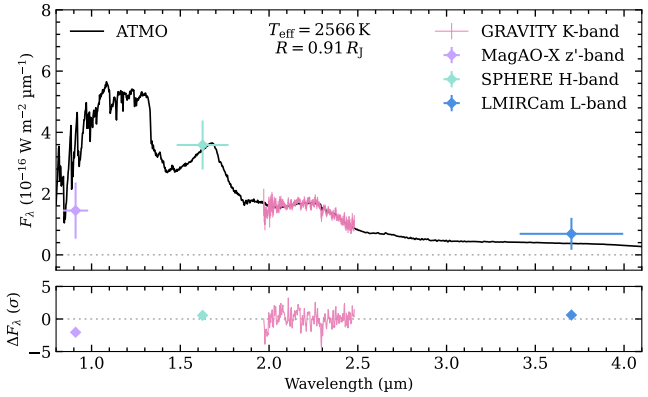

(f) `ATMO` **best fit spectrum with inferred planet temperature and radius.**

Figure 13. Exploration of multiple model grids.

ORCID iDs

Chloe Lawlor https://orcid.org/0009-0001-0368-1062
Richelle F. van Capelleveen https://orcid.org/0009-0002-6729-646X
Guillaume Bourdarot https://orcid.org/0000-0002-6777-6386
Christian Ginski https://orcid.org/0000-0002-4438-1971
Matthew A. Kenworthy https://orcid.org/0000-0002-7064-8270
Tomas Stolker https://orcid.org/0000-0002-5823-3072
Laird Close https://orcid.org/0000-0002-2167-8246
Alexander J. Bohn https://orcid.org/0000-0003-1401-9952
Paulo Garcia https://orcid.org/0000-0002-1678-3535
Sebastian F. Hönig https://orcid.org/0000-0002-6353-1111
Jens Kammerer https://orcid.org/0000-0003-2769-0438
Laura Kreidberg https://orcid.org/0000-0003-0514-1147
Sylvestre Lacour https://orcid.org/0000-0002-6948-0263
Jean-Baptiste Le Bouquin https://orcid.org/0000-0002-0493-4674
Eric Mamajek https://orcid.org/0000-0003-2008-1488
Thibaut Paumard https://orcid.org/0000-0003-0655-0452
Christian Straubmeier https://orcid.org/0000-0002-0671-9302
Nienke van der Marel https://orcid.org/0000-0003-2458-9756

References

Allard, F. 2014, IAUS, 299, 271
Allard, F., Homeier, D., & Freytag, B. 2012, RSPTA, 370, 2765
Allers, K. N., & Liu, M. C. 2013, ApJ, 772, 79
Andrews, S. M., Huang, J., Pérez, L. M., et al. 2018, ApJL, 869, L41
Avenhaus, H., Quanz, S. P., Garufi, A., et al. 2018, ApJ, 863, 44
Baron, E., Hauschildt, P. H., Allard, F., et al. 2003, IAUS, 210, 19
Baudino, J.-L., Bézard, B., Boccaletti, A., et al. 2015, A&A, 582, A83
Beuzit, J.-L., Vigan, A., Mouillet, D., et al. 2019, A&A, 631, A155
Blunt, S., Wang, J. J., Angelo, I., et al. 2020, AJ, 159, 89
Boss, A. P. 1997, Sci, 276, 1836
Bourdarot, G., Eisenhauer, F., Yazıcı, S., et al. 2024, arXiv:2409.08438
Cesetti, M., Pizzella, A., Ivanov, V. D., et al. 2013, A&A, 549, A129
Charnay, B., Bézard, B., Baudino, J.-L., et al. 2018, ApJ, 854, 172
Close, L. M., Males, J. R., Li, J., et al. 2025b, AJ, 169, 35
Close, L. M., van Capelleveen, R. F., Weible, G., et al. 2025a, ApJL, 990, L9
Currie, T., Biller, B., Lagrange, A., et al. 2023, ASPC, 534, 799
Currie, T., Lawson, K., Schneider, G., et al. 2022, NatAs, 6, 751
Cutri, R. M., Skrutskie, M. F., van Dyk, S., et al. 2003, 2MASS All Sky Catalog of Point Sources (NASA/IPAC Infrared Science Archive)
Dohlen, K., Langlois, M., Saisse, M., et al. 2008, SPIE, 7014, 70143L
Dong, R., Hashimoto, J., Rafikov, R., et al. 2012, ApJ, 760, 111
Ercolano, B., Mayr, D., Owen, J. E., Rosotti, G., & Manara, C. F. 2014, MNRAS, 439, 256
Flock, M., Nelson, R. P., Turner, N. J., et al. 2017, ApJ, 850, 131
Foreman-Mackey, D., Conley, A., Meierjurgen Farr, W., et al. 2013, emcee: The MCMC Hammer, Astrophysics Source Code Library, ascl:1303.002
Gaia Collaboration, Vallenari, A., Brown, A. G. A., et al. 2023, A&A, 674, A1
Garufi, A., Ginski, C., van Holstein, R. G., et al. 2024, A&A, 685, A53
Ginski, C., Garufi, A., Benisty, M., et al. 2024, A&A, 685, A52
GRAVITY+ Collaboration 2026, A&A, 707, A115
GRAVITY Collaboration, Abuter, R., Accardo, M., et al. 2017, A&A, 602, A94
GRAVITY Collaboration, Lacour, S., Nowak, M., et al. 2019, A&A, 623, L11
Gregorio-Hetem, J., Lepine, J. R. D., Quast, G. R., Torres, C. A. O., & de La Reza, R. 1992, AJ, 103, 549
Haffert, S. Y., Bohn, A. J., de Boer, J., et al. 2019, NatAs, 3, 749
Hammond, I., Christiaens, V., Price, D. J., et al. 2023, MNRAS, 522, L51
Hashimoto, J., Dong, R., Kudo, T., et al. 2012, ApJL, 758, L19
Hashimoto, J., Tsukagoshi, T., Brown, J. M., et al. 2015, ApJ, 799, 43
Hauschildt, P. H., & Baron, E. 1999, JCoAM, 109, 41
Helling, C., Dehn, M., Woitke, P., & Hauschildt, P. H. 2008a, ApJL, 675, L105
Helling, C., & Woitke, P. 2006, A&A, 455, 325
Helling, C., Woitke, P., & Thi, W.-F. 2008b, A&A, 485, 547
Kammerer, J., Winterhalder, T. O., Lacour, S., et al. 2025, A&A, 704, A318
Keppler, M., Benisty, M., Müller, A., et al. 2018, A&A, 617, A44
Keppler, M., Teague, R., Bae, J., et al. 2019, A&A, 625, A118
Kurtovic, N. T., Pérez, L. M., Benisty, M., et al. 2018, ApJL, 869, L44
Kuznetsova, A., Bae, J., Hartmann, L., & Mac Low, M.-M. 2022, ApJ, 928, 92
Lapeyrere, V., Kervella, P., Lacour, S., et al. 2014, SPIE, 9146, 91462D
Limbach, M. A., & Turner, E. L. 2015, PNAS, 112, 20
Lissauer, J. J., Batalha, N. M., & Borucki, W. J. 2023, ASPC, 534, 839
MacKay, D. J. C. 2003, Information Theory, Inference, and Learning Algorithms (Cambridge Univ. Press)
Manara, C. F., Ansdell, M., Rosotti, G. P., et al. 2023, ASPC, 534, 539
Manara, C. F., Frasca, A., Venuti, L., et al. 2021, A&A, 650, A196
Marcus, P. S., Pei, S., Jiang, C.-H., et al. 2015, ApJ, 808, 87
Marley, M. S., Saumon, D., Visscher, C., et al. 2021, ApJ, 920, 85
Marley, M. S., & Sengupta, S. 2011, MNRAS, 417, 2874
Marois, C., Macintosh, B., Barman, T., et al. 2008, Sci, 322, 1348
Milli, J., Mouillet, D., Lagrange, A.-M., et al. 2012, A&A, 545, A111
Morley, C. V., Mukherjee, S., Marley, M. S., et al. 2024, ApJ, 975, 59
Nasedkin, E., Mollière, P., Lacour, S., et al. 2024, A&A, 687, A298
Nowak, M., Lacour, S., Lagrange, A.-M., et al. 2020, A&A, 642, L2
Öberg, K. I., Guzmán, V. V., Walsh, C., et al. 2021, ApJS, 257, 1
Patience, J., King, R. R., De Rosa, R. J., et al. 2012, A&A, 540, A85
Perotti, G., Christiaens, V., Henning, T., et al. 2023, Natur, 620, 516
Phillips, M. W., Tremblin, P., Baraffe, I., et al. 2020, A&A, 637, A38
Pollack, J. B., Hubickyj, O., Bodenheimer, P., et al. 1996, Icar, 124, 62
Rajpurohit, A. S., Reylé, C., Schultheis, M., et al. 2012, A&A, 545, A85
Rukdee, S. 2024, NatSR, 14, 27356
Schneider, J., Dedieu, C., Le Sidaner, P., Savalle, R., & Zolotukhin, I. 2011, A&A, 532, A79
Speagle, J. S. 2020, MNRAS, 493, 3132
Spiegel, D. S., & Burrows, A. 2012, ApJ, 745, 174
Stolker, T., Marleau, G.-D., Cugno, G., et al. 2020a, A&A, 644, A13
Stolker, T., Quanz, S. P., Todorov, K. O., et al. 2020b, A&A, 635, A182
Suriano, S. S., Li, Z.-Y., Krasnopolsky, R., & Shang, H. 2018, MNRAS, 477, 1239
Trevascus, D., Blunt, S., Christiaens, V., et al. 2025, A&A, 698, A19
van Capelleveen, R. F., Ginski, C., Kenworthy, M. A., et al. 2025, ApJL, 990, L8
Wang, J. J., Vigan, A., Lacour, S., et al. 2021, AJ, 161, 148
Witte, S., Helling, C., Barman, T., Heidrich, N., & Hauschildt, P. H. 2011, A&A, 529, A44
Witte, S., Helling, C., & Hauschildt, P. H. 2009, A&A, 506, 1367
Woitke, P., & Helling, C. 2003, A&A, 399, 297
Woitke, P., & Helling, C. 2004, A&A, 414, 335
Xie, J.-W., Dong, S., Zhu, Z., et al. 2016, PNAS, 113, 11431
Zhou, Y., Bowler, B. P., Sanghi, A., et al. 2025, ApJL, 980, L39